Development of a Two-Dimensional Finite-Element PBL Model and Two Preliminary Model Applications[1]

L. P. CHANG[2] AND E. S. TAKLE

Departments of Earth Sciences and Agronomy, Iowa State University, Ames 50011

R. L. SANI

Cooperative Institute for Research in Environmental Sciences, University of Colorado, Boulder 80309

(Manuscript received 20 August 1981, in final form 29 July 1982)

ABSTRACT

We have developed a two-dimensional finite-element model for simulating atmospheric flow in the planetary boundary layer (PBL) of the earth. The finite-element method provides a useful alternative to the conventional finite-difference method in studying flow phenomena that involve graded meshes and (or) irregular computational domains. It also provides a more natural way of incorporating Dirichlet-type boundary conditions. These properties make the finite-element method especially suitable for studying PBL flows. With the Deardorff–O'Brien turbulence scheme, the model was able to generate reasonable results in the simulations of a neutral PBL wind profile and a sea-breeze circulation.

1. Introduction

We have developed a two-dimensional finite-element (FE) model for simulating atmospheric flow in the earth's planetary boundary layer (PBL). Wang *et al.* (1972), Cullen (1973), Gresho *et al.* (1976), Staniforth and Mitchell (1977), Manton (1978a,b), Staniforth and Daley (1979), and Lee and Kao (1979) have described applications and advantages of the FE method for meteorological problems. The FE method (Zienkiewicz, 1977) incorporates graded meshes, irregular computational domains, and boundary conditions in a quite different manner from the more conventional finite-difference (FD) method, and for certain problems has greater accuracy than equal or even higher-order FD approximations (Cullen, 1973; Haltiner and Williams, 1980). These differences could give the FE method an advantage over FD methods for modeling the PBL. The FE method only recently has been used for PBL modeling, and hence many of the potential advantages of the FE method (e.g., strongly graded meshes for resolving frontal zones, dynamically adjusting grids, logarithmic boundary elements at the earth's surface, ease of mapping over irregular terrain) have yet to be more thoroughly studied before the full potential of the method can be assessed and perhaps exploited for atmospheric flows.

The purpose of the research reported here was to apply the FE method to a well-studied mesoscale flow, not only for comparison with observations and other models, but also to provide a starting point for studying certain capabilities of the FE method that may be exploited for modeling the PBL. The use of such features as logarithmic interpolation functions near the surface, strongly graded meshes, dynamic meshes, and alternative boundary condition specification over irregular terrain are subjects of present and future research and will be subjects of future reports. The present model provides a basic framework within which these alternatives can be evaluated.

2. Model description

The present model is an extension of the two-dimensional (2-D) finite-element model developed by Chan *et al.* (1980).

a. Governing equations

The governing equations are the hydrostatic shallow-convection Boussinesq equations. The dependent variables used are u, v, w, θ and π, which are the three velocity components, the potential temperature, and the Exner pressure function. The potential temperature and the pressure are decomposed into a steady basic-state component, denoted by subscript zero, and a deviation, denoted by a prime:

$$\theta = \theta_0 + \theta', \quad \pi = \pi_0 + \pi'.$$

The basic state is characterized by an adiabatic tem-

[1] Journal Paper No. J-10340 of the Iowa Agriculture and Home Economics Experiment Station, Ames. Project No. 2116.

[2] Present address: Cooperative Institute for Research in Mesoscale Meteorology, University of Oklahoma, Norman, OK 73019.

0027-0644/82/122025-13$07.25

perature stratification and a hydrostatic pressure distribution. Thus, the governing equations expressed in u, v, w, θ', and π' take the form

$$\frac{\partial u}{\partial t} = -u\frac{\partial u}{\partial x} - w\frac{\partial u}{\partial z} - \theta_0\frac{\partial \pi'}{\partial x} + \frac{\partial}{\partial x}\left(K_x^m\frac{\partial u}{\partial x}\right) + \frac{\partial}{\partial z}\left(K_z^m\frac{\partial u}{\partial z}\right) + f(v - v_g), \quad (1)$$

$$\frac{\partial v}{\partial t} = -u\frac{\partial v}{\partial x} - w\frac{\partial v}{\partial z} + \frac{\partial}{\partial x}\left(K_x^m\frac{\partial v}{\partial x}\right) + \frac{\partial}{\partial z}\left(K_z^m\frac{\partial v}{\partial z}\right) + f(u_g - u), \quad (2)$$

$$\frac{\partial \pi'}{\partial z} = \frac{\theta'}{\theta_0^2}g, \quad (3)$$

$$\frac{\partial u}{\partial x} + \frac{\partial w}{\partial z} = 0, \quad (4)$$

$$\frac{\partial \theta'}{\partial t} = -u\frac{\partial \theta'}{\partial x} - w\frac{\partial \theta'}{\partial z} + \frac{\partial}{\partial x}\left(K_x^h\frac{\partial \theta'}{\partial x}\right) + \frac{\partial}{\partial z}\left(K_z^h\frac{\partial \theta'}{\partial z}\right), \quad (5)$$

where the following assumptions have been employed:

1) The y-derivative of any quantity is zero, except for the large-scale pressure π_0, which is given by the geostrophic wind equations.

2) The geostrophic wind is assumed to be steady and not to vary with height.

The determination of the vertical exchange coefficients for momentum and heat, K_z^m and K_z^h, is based on O'Brien's exchange-coefficient profile (O'Brien, 1970), together with Businger's formulas for the wind and temperature profiles as a function of stability in the surface layer (Businger, 1973) and Deardorff's semi-empirical formula for the growth of the PBL (Deardorff, 1974). A detailed discussion of this turbulence scheme is given by Pielke and Mahrer (1975). The horizontal diffusion terms are included for damping numerical noise. The value of K_x^m ($=K_x^h$) is experimentally determined to be just large enough to retain computational stability. A brief discussion of the effect of K_x on the vertical velocity field is given in Section 4.

b. Finite-element approximation

The finite-element approximation of the governing equations employs the following expansions in an element:

$$q(t, x, z) \approx \tilde{q}(t, x, z) \equiv \sum_{i=1}^{9} \hat{q}_i(t)\Psi_i(x, z), \quad (6)$$

$$\overline{\pi'}(t, x, z) \approx \tilde{\pi}'(t, x, z) \equiv \sum_{i=1}^{4} \hat{\pi}'(t)\phi_i(x, z), \quad (7)$$

where q represents any of the four dependent variables u, v, w or θ'; Ψ's represent the nine-node bi-quadratic shape functions; and ϕ's represent the shape functions for pressure, either bi-quadratic or bi-linear. We have used the nine-node bi-quadratic elements for reasons discussed by Huyakorn *et al.* (1978), and also for eventual use for modeling flows over irregular terrain where the quadratic function will give a better representation of curved boundaries.

For non-hydrostatic models, it is desirable to use a mixed interpolation, with the interpolation for pressure an order lower than for velocity or temperature to avoid the generation of a spurious pressure mode in the solution (Hood and Taylor, 1974; Sani *et al.*, 1980). For a hydrostatic model, pressure is directly determined from integration of the buoyancy force in the z-direction, thereby eliminating the need for a lower-order pressure interpolation.

The Galerkin method is applied to the prognostic equations (1), (2) and (5), and, to create symmetric matrices, the least-squares method is applied to the diagnostic equations (3) and (4). To linearize the advection terms, we assume that the advective velocities are known from the most-updated values so that, at any given time, they are treated as known quantities.

By substitution of Eqs. (6) and (7) into (1)–(5), multiplication by appropriate shape functions as weights, and integration over an element domain Ω_e, we obtain the following element equations:

$$\sum_{i=1}^{9}\left[\frac{d\hat{u}_i}{dt}\iint_{\Omega_e}\Psi_i\Psi_j dA + \hat{u}_i\iint_{\Omega_e}\left(u\Psi_j\frac{\partial\Psi_i}{\partial x} + w\Psi_j\frac{\partial\Psi_i}{\partial z} + K_x^m\frac{\partial\Psi_i}{\partial x}\frac{\partial\Psi_j}{\partial x} + K_z^m\frac{\partial\Psi_i}{\partial z}\frac{\partial\Psi_j}{\partial z}\right)dA\right]$$
$$= \sum_{i=1}^{9}\iint_{\Omega_e}\hat{v}_i\Psi_i f\Psi_j dA + \int_{\partial\Omega_{e_1}}\Psi_j\left(K_x^m\frac{\partial u}{\partial x}n_x + K_z^m\frac{\partial u}{\partial z}n_z\right)dl - \sum_{k=1}^{4}\theta_0\pi'_k\iint_{\Omega_e}\Psi_j\frac{\partial\phi_k}{\partial x}dA - \iint_{\Omega_e}fv_g\Psi_j dA, \quad (8)$$

$$\sum_{i=1}^{9}\left[\frac{d\hat{v}_i}{dt}\iint_{\Omega_e}\Psi_i\Psi_j dA + \hat{v}_i\iint_{\Omega_e}\left(u\Psi_j\frac{\partial\Psi_i}{\partial x} + w\Psi_j\frac{\partial\Psi_i}{\partial z} + K_x^m\frac{\partial\Psi_i}{\partial x}\frac{\partial\Psi_j}{\partial x} + K_z^m\frac{\partial\Psi_i}{\partial z}\frac{\partial\Psi_j}{\partial z}\right)dA\right]$$
$$= -\sum_{i=1}^{9}\iint_{\Omega_e}\hat{u}_i\Psi_i f\Psi_j dA + \int_{\partial\Omega_{e_1}}\Psi_j\left(K_x^m\frac{\partial v}{\partial x}n_x + K_z^m\frac{\partial v}{\partial z}n_z\right)dl - \sum_{k=1}^{4}\theta_0\hat{\pi}'_k\iint_{\Omega_e}\Psi_j\frac{\partial\phi_k}{\partial y}dA + \iint_{\Omega_e}fu_g\Psi_j dA, \quad (9)$$

$$\sum_{i=1}^{4} \hat{\pi}'_i \iint_{\Omega_e} \frac{\partial \phi_i}{\partial z} \frac{\partial \phi_j}{\partial z} dA = \sum_{k=1}^{9} \frac{1}{\theta_0^2} g\theta'_k \iint_{\Omega_e} \frac{\partial \phi_j}{\partial z} \Psi_k dA (j = 1, 2, 3, 4), \quad (10)$$

$$\sum_{i=1}^{9} \hat{w}_i \iint_{\Omega_e} \frac{\partial \Psi_i}{\partial z} \frac{\partial \Psi_j}{\partial z} dA = -\sum_{k=1}^{9} \hat{u}_k \iint_{\Omega_e} \frac{\partial \Psi_k}{\partial z} \frac{\partial \Psi_j}{\partial x} dA (j = 1, 2, \ldots, 9), \quad (11)$$

$$\sum_{i=1}^{9} \left[\frac{d\hat{\theta}_i}{dt} \iint_{\Omega_e} \Psi_i \Psi_j dA + \hat{\theta}'_i \iint_{\Omega_e} \left(u\Psi_j \frac{\partial \Psi_i}{\partial x} + w\Psi_j \frac{\partial \Psi_i}{\partial z} + K_x^h \frac{\partial \Psi_i}{\partial x} \frac{\partial \Psi_j}{\partial x} + K_z^h \frac{\partial \Psi_i}{\partial z} \frac{\partial \Psi_j}{\partial z} \right) dA \right] = \int_{\partial \Omega_{e_2}} \Psi_j \left(K_x^h \frac{\partial \theta'}{\partial x} n_x + K_z^h \frac{\partial \theta'}{\partial z} n_z \right) \times dl (j = 1, 2, \ldots, 9). \quad (12)$$

Diffusion terms have been integrated by parts (see Zienkiewicz, 1977). Here, Ω_e represents an element domain, and Ω_{e_1} and Ω_{e_2}, respectively, represent those portions of the boundary of an element on which normal derivative of velocity and potential temperature are defined.

The set of five approximate governing equations can be cast into a more compact form by use of the following notation:

$$(\hat{\mathbf{u}})^t = \{\hat{u}_1 \hat{u}_2 \cdots \hat{u}_9\},$$
$$(\hat{\mathbf{v}})^t = \{\hat{v}_1 \hat{v}_2 \cdots \hat{v}_9\},$$
$$(\hat{\theta}')^t = \{\hat{\theta}'_1 \hat{\theta}'_2 \cdots \hat{\theta}'_9\},$$
$$(\hat{\mathbf{w}})^t = \{\hat{w}_1 \hat{w}_2 \cdots \hat{w}_9\},$$
$$(\hat{\pi}')^t = \{\hat{\pi}'_1 \hat{\pi}'_2 \hat{\pi}'_3 \hat{\pi}'_4\},$$
$$(\hat{\mathbf{U}})^t = \{(\hat{\mathbf{u}})^t (\hat{\mathbf{w}})^t\},$$
$$\hat{\mathbf{q}} = \hat{\mathbf{u}}, \hat{\mathbf{v}}, \text{ or } \hat{\theta}',$$
$$\hat{\mathbf{x}} = \hat{\pi}' \text{ or } \hat{\mathbf{w}}.$$

We then can write Eqs. (8), (9) and (12) as

$$\mathbf{M}\dot{\hat{q}} + \mathbf{C}(\mathbf{U})\hat{\mathbf{q}} + \mathbf{k}\hat{\mathbf{q}} = \mathbf{F}, \quad (13)$$

and Eqs. (10) and (11) as

$$\mathbf{AX} = \mathbf{B}, \quad (14)$$

c. Modified Crank-Nicholson time-differencing scheme

We use a modified Crank-Nicholson method to convert the ordinary differential equations in time to algebraic equations. By this method, Eq. (13) is written as

$$\frac{1}{\Delta t}\mathbf{M}(\hat{\mathbf{q}}^{n+1} - \hat{\mathbf{q}}^n) + \mathbf{C}(\hat{\mathbf{U}}^n)\hat{\mathbf{q}}^{n+1/2} + \mathbf{K}\hat{\mathbf{q}}^{n+1/2} = \mathbf{F}^n. \quad (15)$$

This equation can be rewritten as

$$\left[\frac{2}{\Delta t}\mathbf{M} + \mathbf{C}(\hat{\mathbf{U}}^n) + \mathbf{K}\right]\hat{\mathbf{q}}^{n+1/2} = \mathbf{F}^n + \frac{2}{\Delta t}\mathbf{M}\hat{\mathbf{q}}^n, \quad (16)$$

and used to solve for $\hat{\mathbf{q}}^{n+1/2}$. After $\hat{\mathbf{q}}^{n+1/2}$ has been obtained, we then calculate $\hat{\mathbf{q}}^{n+1}$ from

$$\hat{\mathbf{q}}^{n+1} = 2\hat{\mathbf{q}}^{n+1/2} - \hat{\mathbf{q}}^n. \quad (17)$$

Similarly, we solve Eq. (14) by first using the most updated $\hat{\mathbf{u}}^{n+1/2}$ and $\hat{\theta}'^{n+1/2}$ to calculate the rhs vector $\mathbf{B}$. Then we find $\hat{\mathbf{x}}^{n+1/2}$ by solving

$$\mathbf{A}\hat{x}^{n+1/2} = \mathbf{B}^{n+1/2}. \quad (18)$$

Finally, we calculate $\hat{\mathbf{x}}$ from

$$\hat{\mathbf{x}}^{n+1} = 2\hat{\mathbf{x}}^{n+1/2} - \mathbf{x}^n. \quad (19)$$

Notice that, although we have only diagnostic equations for $\hat{\mathbf{w}}$ and $\hat{\pi}$, $\hat{\mathbf{x}}^{n+1}$ is, nevertheless, dependent on $\hat{\mathbf{x}}^n$.

d. Solution procedure

After the element equations are assembled into the global algebraic equation in $\hat{\mathbf{u}}_g$, $\hat{\mathbf{v}}_g$, $\hat{\mathbf{w}}_g$, $\hat{\theta}'_g$ and $\hat{\pi}'_g$, where the subscript g denotes that these dependent variables now represent global vectors, the global nodal values of the five dependent variables are solved in a block-iterative manner, so that, for each iteration, only one dependent variable is unknown, the other four taking on their most updated values. Convergence is defined when the relative errors between two successive iterations are less than the specified error bounds (10^{-5} for the seabreeze study). Thus, for each time step, we iterate over the five global dependent-variable vectors $\hat{\mathbf{u}}$, $\hat{\mathbf{v}}_g$, $\hat{\mathbf{w}}_g$, $\hat{\theta}'_g$, and $\hat{\pi}'_g$ until they all have achieved convergence. The vertical exchange coefficients K_z^m and K_z^h are computed from the profiles of velocity and temperature of the previous time step.

3. Model simulation of the steady-state wind profile for a neutral horizontally homogeneous PBL

The first application of our model is the simulation of the steady-state wind profile for a neutral horizontally homogeneous PBL. The steady-state solution is approached by running the model through several inertial periods until the relative radius of the inertial circle was ±0.02.

To prevent distortion of the wind profiles in the upper part of the PBL arising from the influence of the top boundary, we have used a domain height zf/u_* of ~1.2. The computational domain consists of a column of nine-node bi-quadratic elements, although for 1-D studies, the horizontal aspect is irrelevant. The element vertical dimensions increase al-

most logarithmically from a few z_0 to several meters at 50 m, and almost linearly from 50 to 500 m.

The mean wind at the top of the domain and the surface roughness length z_0, are both specified. To compare our results with models that specify a surface stress, we make the following transformation:

$$\left.\begin{aligned} u_s &= u\cos A + v\sin A \\ v_s &= -u\sin A + v\cos A \\ A_s &= \tan(v/u)_{\text{sfc}}, \end{aligned}\right\} \quad (20)$$

where values at the first level above the ground are used to determine the surface cross-isobaric angle A, and u_s at this level gives the surface wind and the direction of the surface stress.

With a geostrophic wind of 10 m s^{-1}, a roughness length of 0.01 m, and a surface-layer depth of 0.01 u_*/f, the model is run to approach the steady-state wind profile. The resulting velocity components are converted to u_s and v_s by using Eq. (20). A plot of u_s/u_* and v_s/u_*, respectively normalized by values of u_s/u_* and v_s/u_* evaluated at the nondimensional height $zf/u_* = 1$, are given in Fig. 1. Also shown in this figure are the corresponding curves from model results of Shir (1973), Wyngaard *et al.* (1974) and Zeman and Tennekes (1975). The general shapes of these profiles agree reasonably well with other model results where higher-order turbulence closure schemes are employed.

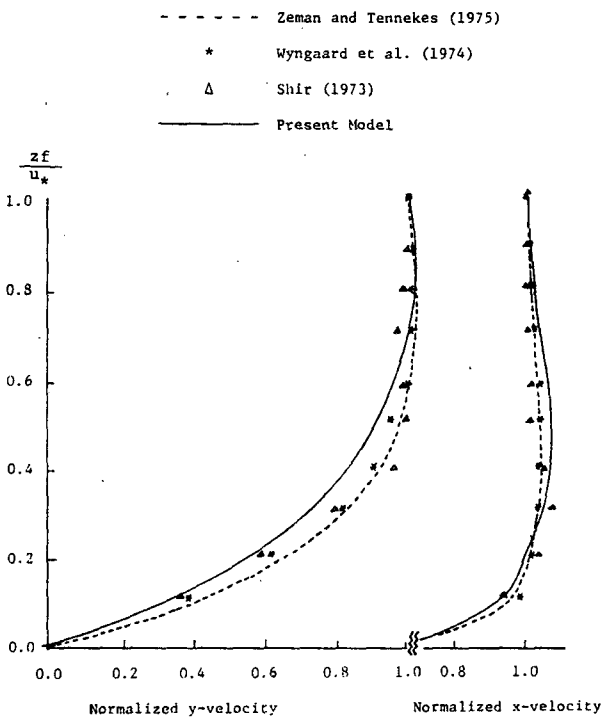

FIG. 1. Vertical profiles of horizontal velocities normalized by u_s/u_* at $(zf)/u_* = 1$ for the x-component and v_c/u_* at $(zf)/u_* = 1$ for the y-component.

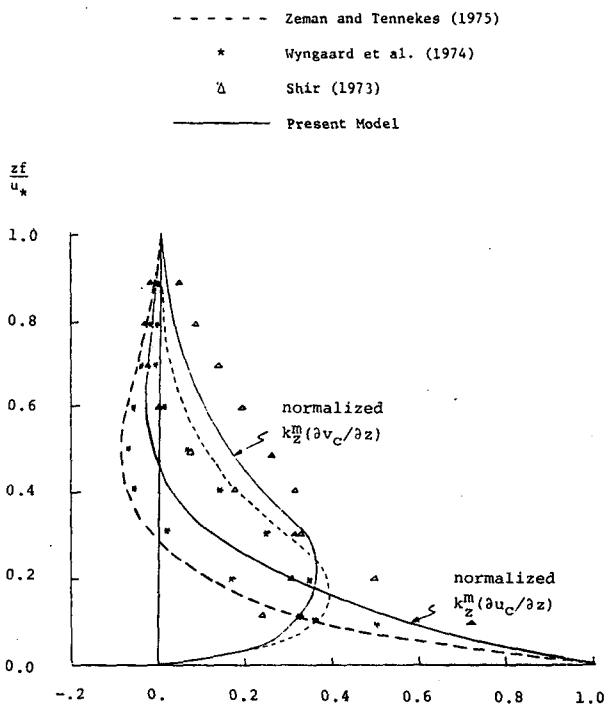

FIG. 2. Nondimensional profiles of the stresses $K_z^m(\partial u_c/\partial z)$ and $K_z^m(\partial v_c/\partial z)$ normalized by their surface values, respectively.

Estimates of the horizontal stresses $\overline{u'w'}$ and $\overline{v'w'}$ are obtained by computing $K_z^m(\partial u_s/\partial z)$ and $K_z^m(\partial v_s/\partial z)$, using centered differencing for the derivatives. Nondimensional vertical profiles of these two quantities, each normalized by its own surface value, are shown in Fig. 2. The normalized stresses, $\overline{u'w'}/u_*^2$ and $\overline{v'w'}/u_*^2$, from the aforementioned models also are presented for comparison. Again, the shapes of the horizontal stresses are in general agreement with results of the more sophisticated turbulence models.

The momentum equations, when integrated for a long time to achieve the steady-state profiles, produce the expected inertial oscillation in the velocity solution. In the Northern Hemisphere, the Coriolis deflection causes the inertial motion to be in a clockwise sense, with a period of $2\pi/f$, approximately 17 h at 45°N. If friction is negligible, the horizontal wind retains its speed c; thus, $u^2 + v^2 = c^2$. When the friction is given by $(\partial/\partial z)(K_z^m \partial u/\partial z)$ for u and $(\partial/\partial z)(K_z^m \partial v/\partial z)$ for v, the u- and v-components will follow a quasi-circular path to eventually converge to their equilibrium values.

A plot of the normalized u and v components for two different heights (10.7 and 1043 m) is shown in Fig. 3 to illustrate the inertial oscillation for a total time of 27.7 h. The period of the inertial oscillation is seen to be ~17 h, in agreement with the theoretical value of $2\pi/f$ for 45°N latitude. Also, the two inertial circles are seen to be in phase, indicating that the motion in the entire vertical column already is well coupled.

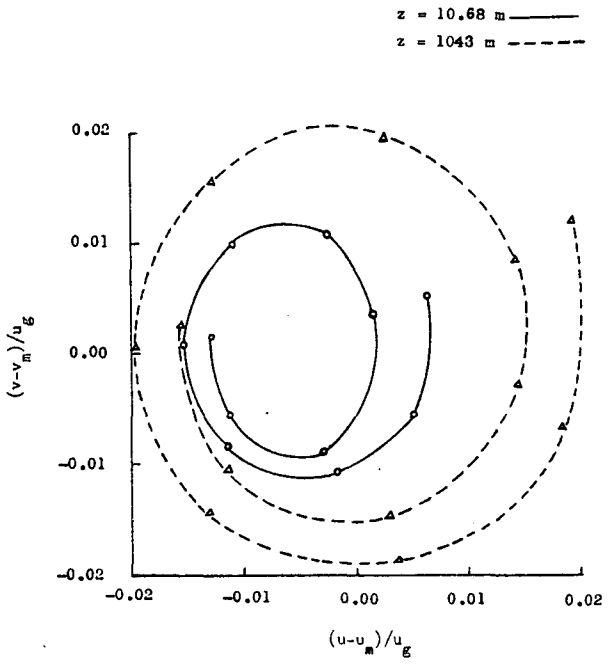

FIG. 3. Inertial circles at two different levels (10.68 and 1043 m) in the calculation of a 1-D steady-state wind profile. The geostrophic wind speed is 10 m s^{-1} at the upper boundary, and the roughness length is 0.01 m. u_m and v_m represent characteristic values of u and v at a given height. They are, respectively, 6.490 and 1.022 m s^{-1} for z = 10.68 m, and 10.096 and 0.500 m s^{-1} for z = 1043 m. The time interval between two successive points is approximately 2.52 h.

4. Model application to the sea-breeze circulation

The sea-breeze circulation provides a convenient mesoscale flow for testing the two-dimensional capabilities of the model because it has been studied relatively well both observationally and theoretically. This circulation also affords opportunities for evaluating model performance on a variety of spatial scales, ranging from the large primary vortex to small-scale features in the vicinity of the sea-breeze front. The following items will be used to examine the model performance in simulating the sea breeze:

1) The generation of the sea-breeze inflow at low levels and the formation of a weaker return flow aloft. 2) The depth and inland displacement of the sea-breeze inflow at the mature stage of the sea breeze. 3) The intensity and the inland movement of the position of the maximum updraft as a function of time. 4) The rate of the inland penetration of the sea-breeze front defined by the wind-shift line, $u = 0$, near the surface, by the horizontal position of the maximum updraft, or by the minimum surface pressure. 5) The upward distortion of the isotherms (isentropes) in the frontal zone. 6) The change in wind direction and speed with time at a given station on land due to frontal passage and the Coriolis deflection. 7) The evolution of the surface pressure pattern. 8) The influence of an offshore synoptic wind on the strength and spatial extent of the sea-breeze circulation.

a. Domain discretization and the initial and boundary conditions

The computational domain is rectangular, 109 km in the horizontal and 2500 m high. In order to resolve the frontal movement reasonably well, we discretize the domain into 17 × 6 rectangular bi-quadratic elements with an effective horizontal grid spacing of 2.5 km, spanning a length of ~30 km inland from the shore. Outside this area, the horizontal resolution is halved. In the presence of an offshore synoptic wind, the sea breeze is more limited to the coastal area, a typical penetration being 5 to 10 km inland. Therefore, we use a 1 km horizontal resolution to span a shorter inland penetration zone for the offshore wind simulation.

The initial potential temperature field is uniform in the horizontal. A neutral layer is assumed for the lowest 200 m, above which there lies a stable layer extending to the top of the domain. The reference potential temperature is taken to be 298 K. The initial velocity field is zero everywhere for the calm case. In the presence of a synoptic wind, a constant x-velocity is applied to the top of the domain. A 1-D (z only) version of the model is run, with a no-slip condition at the bottom, until the velocities at interior nodes reach a steady state for the fixed-temperature profile used. The resultant velocity profile is used as the initial condition for the sea-breeze simulation. As a result of the horizontal homogeneity, the initial vertical velocity is zero. The initial pressure profile is integrated from the vertical distribution of the potential temperature, with $\pi' = 0$ at the top.

The boundary conditions are

Top: u, v, θ' and π' are all invariant with time.

Lateral: The normal derivatives of u, v and θ' vanish.

Bottom: $u = v = w = 0$, $\theta' = A(x) \sin(\pi t/46800 \text{ s})$, following Pielke (1974), where t is time, with $t = 0$ being the onset of the surface differential heating and corresponding to 0800 LST. $A(x)$ is the amplitude function of the heating given by

$$A(x) = \begin{cases} 0 \text{ over water,} \\ 10 \text{ K over land,} \\ \text{linearly decreasing from land to water in the transition zone spanning a length of } 2\Delta x. \end{cases}$$

Other parameters used are $f = 1.0 \times 10^{-4}$ s^{-1}, $g = 9.8$ m s^{-2},

$$z_0 = \begin{cases} 5 \text{ cm over land,} \\ 0.0015 \text{ cm over water,} \\ 1 \text{ cm at the shore for a smooth transition,} \end{cases}$$

and $\Delta t = 60$ s. Numerical experiments indicated that the most appropriate value of the horizontal diffusion coefficient, K_x^m ($=K_x^h$) is 1.5×10^4 m^2 s^{-1}.

In our formulation, we have no top boundary condition on w (our one allowed boundary condition on w is used at the bottom). It could be argued that $\pi' = 0$ is inconsistent with a possible nonzero w at the top. A persistent and horizontally inhomogeneous vertical velocity pattern, even though small in magnitude, would create a significant temperature and pressure disturbance in the stable air near the top over the 10 h of simulated time. However, the w's observed near the top were small and not persistent, and the temperature and pressure fields in the few hundred meters near the top were essentially constant through the simulation. The inconsistency of the $\pi' = 0$ boundary condition, therefore, was judged to have a negligible effect on the sea-breeze circulation that was confined to the lower levels.

b. *Results*

The following model results are for the zero synoptic wind situation. Distortions arising from the large-scale flow are addressed at the end of this section.

1) VELOCITY FIELD

Bi-hourly plots of the u- and w-fields are given in Fig. 4. It can be seen that, soon after the onset of the surface differential heating, a weak sea-breeze circulation is formed. In the lowest 200 m of the circulation, the wind blows onshore, turning to an offshore direction aloft. The maximum offshore wind occurs at a height of 400 m at $t = 2$ h. Because the driving differential heating occurs at the surface, the inflow is initially confined to low levels, with a weaker but deeper return flow aloft as can be seen in Fig. 4. In the vertical, the buoyancy force forms a weak updraft over land and a weaker downdraft over water. It is clear from Fig. 4 that the initial strengths of the updraft and downdraft are approximately the same; the cells of the updraft and the downdraft are quite symmetrical about a vertical line near the coast. This symmetry, however, degenerates as the circulation intensifies. The updraft becomes more concentrated and intense as it moves inland. The downdraft also intensifies and moves inland with time, but at a much slower rate compared with the updraft. Consequently, a region of strong updraft is seen to move inland, with a much wider region of weak downdraft to its seaward side. A noticeable feature for the first few hours is the lack of a distinct frontal zone of the sea-breeze circulation, in the sense that neither a clear wind-shift line nor a sharp horizontal velocity gradient occurs anywhere. For convenience, we may consider the horizontal location of the updraft center as the location of the front.

Sometime between 4 and 5 h, the strong updraft has generated a low-pressure center on the surface due to the distortion of the isotherms in the updraft region. Air is then accelerated horizontally toward the low center. The convergent pattern of the horizontal velocity enhances the updraft, which, in turn, further enhances the horizontal pressure gradient. The pressure gradient force in the sea-ward direction soon generates a region of seaward-blowing wind at low levels some 20 km inland, thereby forming a well-defined front. After the front is established, the updraft intensifies very rapidly and reaches its peak value of $\sim$70 cm s^{-1} sometime between 7 and 8 h (1 to 1.5 h after the maximum surface temperature has occurred). At the same time, the low-level onshore wind shows a maximum of about 7 m s^{-1}.

Numerical experiments with various K_x values revealed very little effect on the velocity fields in the first 4 h of the simulation. Beyond 4 h, the effect was most noticeable in the magnitude of the vertical velocity maximum, which decreased by $\sim$20–30% with a factor of 3 increase in K_x. This suggests that our peak vertical velocity values are likely underestimated. Lyons (1972) reports observations of narrow (1–2 km) convergence bands and updrafts of more than 100 cm s^{-1}. Models such as ours with horizontal grid spacing of 1 km or more are, therefore, not able to give an accurate representation of the maximum updraft speed.

When the effect of the decreasing surface potential temperature becomes dominant, the strength of the sea-breeze circulation begins to diminish, due to the frictional retardation. This weakening is evidenced by the decrease both of the maximum onshore wind and the vertical velocity after 8 h.

2) POTENTIAL TEMPERATURE FIELD

A specific feature of the potential temperature near the sea-breeze front is a strong horizontal gradient of potential temperature formed by an upward movement of the isentropes in that area. The formation of this pattern is a nonlinear process, in that the updraft causes the advection of the isentropes, which enhances the horizontal pressure gradient on the surface. This stronger pressure gradient, in turn, reinforces the updraft to further raise the isentropes. The potential temperature field for $t = 4$, 6, 8, and 10 h in Fig. 5 shows a marked increase in the vertical heat transport after 5 h.

Our model does not show a large drop of low-level potential temperature with the passage of the front that would be expected due to horizontal advection. The reason for this is that the specified land surface potential temperature forces the air immediately above the ground to have nearly the same potential temperature. As a result, the inland advection of the cooler potential temperature is substantially reduced at low levels. Therefore, as pointed out by Pearson

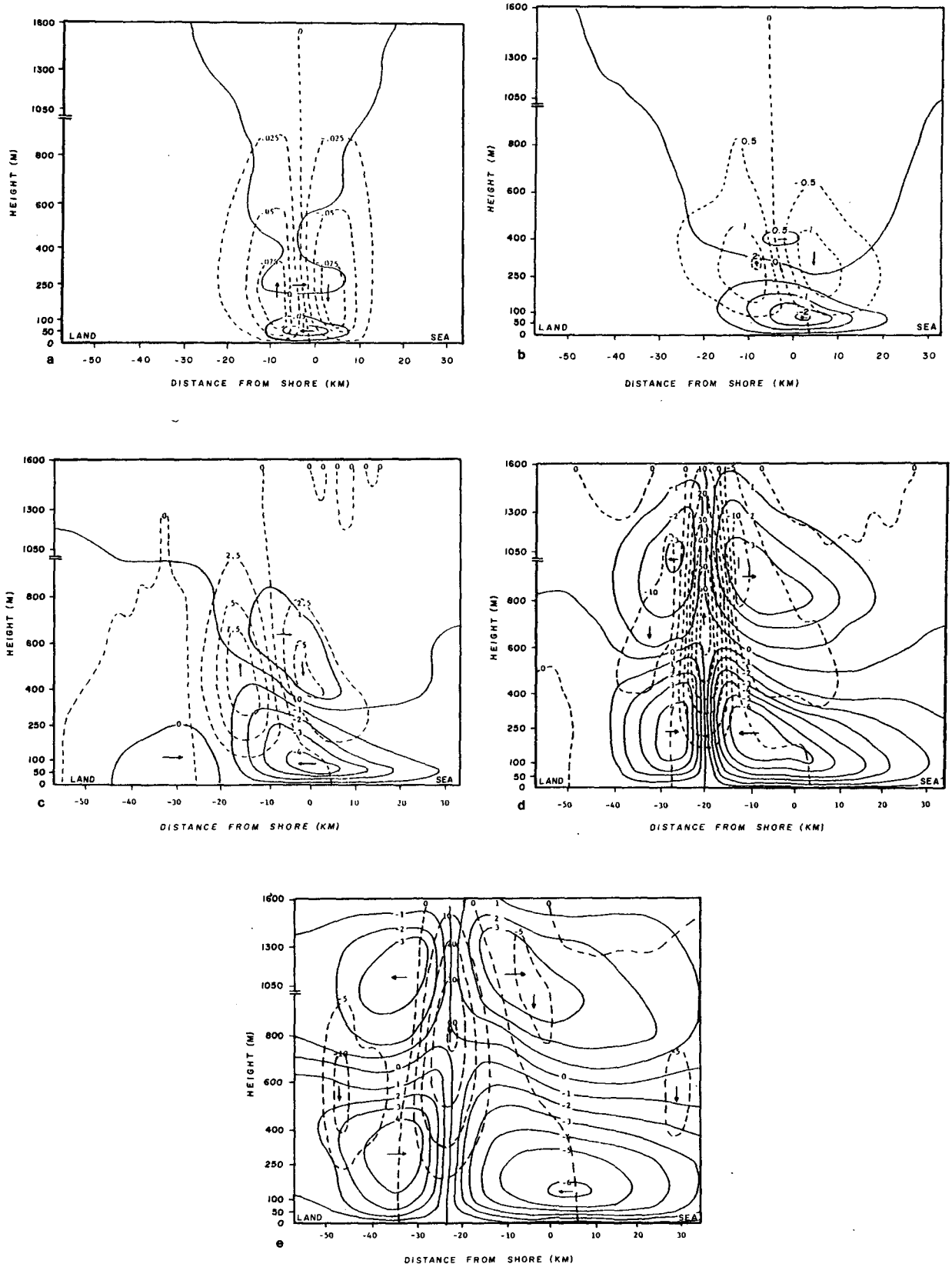

FIG. 4. Computed u (solid line, m s^{-1}) and w (dashed line, cm s^{-1}) for the calm synoptic wind case at (a) t = 1 h, (b) t = 3 h, (c) t = 5 h, (d) t = 7 h, (e) t = 9 h.

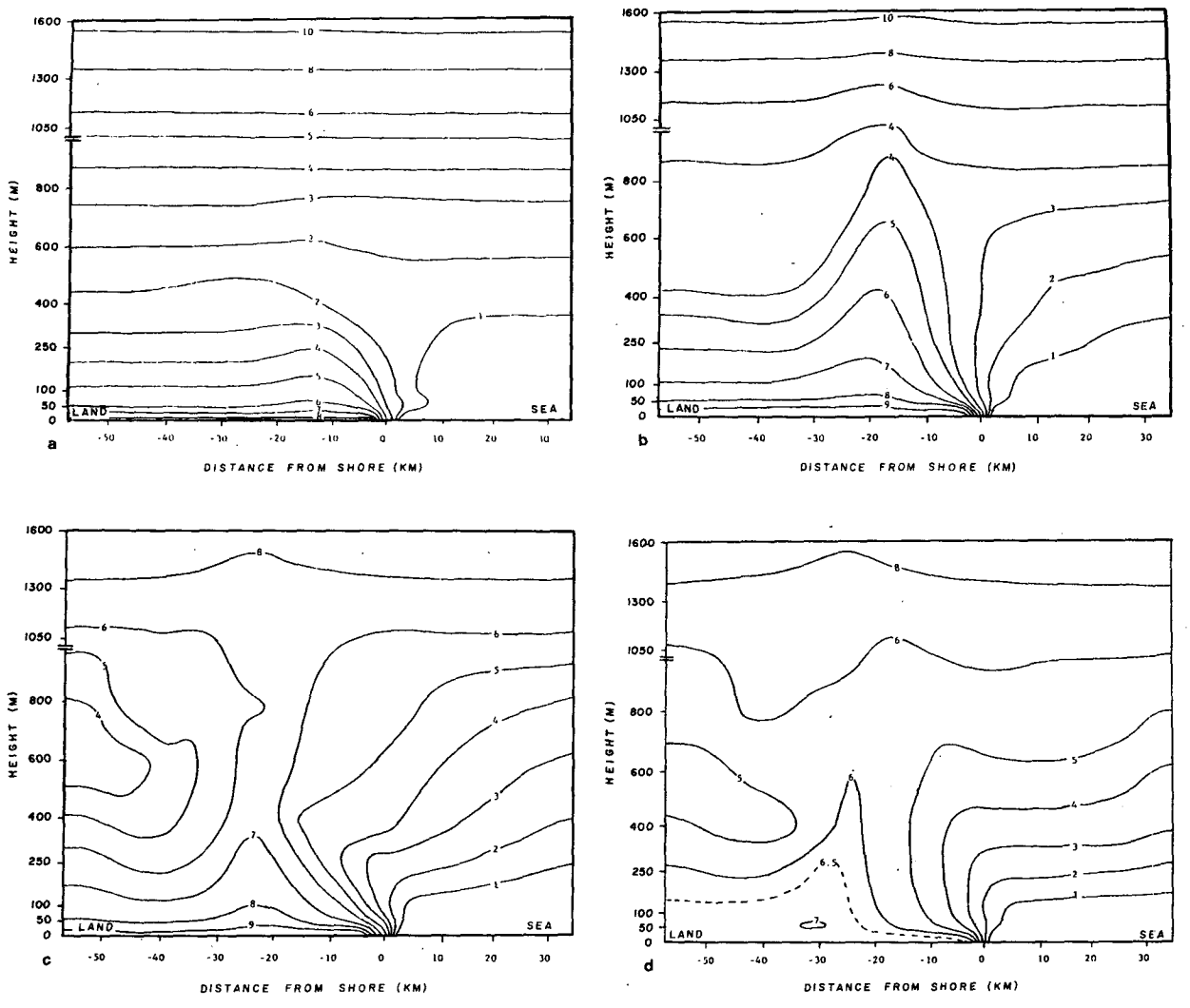

FIG. 5. Computed deviation potential temperature (K) for the calm synoptic wind case at (a) $t = 4$ h, (b) $t = 6$ h, (c) $t = 8$ h, (d) $t = 10$ h.

(1980), "(with the specification of the surface potential temperature), the sea breeze is noticed as a change in wind, although well aloft the temperature may change."

When the peak of the surface potential temperature has passed and the sea breeze begins to diminish, the upward temperature advection also diminishes. The simulation was stopped at 10 h because the stable atmospheric stratification began to set in as the surface temperature continued to drop. With the transition to a stable atmosphere, the height of the convective PBL loses its role as an appropriate turbulence parameter. Consequently, the Deardorff–O'Brien scheme that uses the height of the convective PBL to determine the exchange-coefficient profile should not be applied to simulate the sea-breeze dissipation for late afternoon hours. A scheme that estimates local turbulence characteristics is necessary, because the air near the surface is becoming stable when the overlying air is still likely to be slightly superadiabatic.

3) PRESSURE

The spatial distribution of the pressure for $t = 8$ h is shown in Fig. 6 to illustrate the general pressure pattern in the mature stage of a sea breeze. It is clear from this figure that a low-pressure center on the surface is located near the frontal zone. The associated pressure-gradient force causes the formation of a convergent pattern near the low center at low levels. This induces an updraft near the surface low center. At upper levels, where a stable stratification exists, the rising air is adiabatically cooled and eventually becomes denser than the surrounding air. As a result, the low pressure weakens with height and becomes a high-pressure center aloft. This vertical distribution of pressure is obvious in Fig. 6, and it is this kind of pressure distribution that confines the vertical extent of the sea breeze.

The adjusted surface pressure is plotted in Fig. 7 as a function of time and distance from the shore.

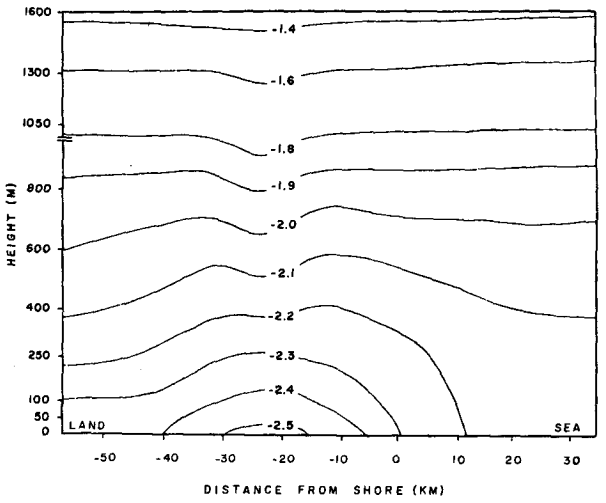

FIG. 6. Computed pressure field in m^2 $(K\ s)^{-1}$ at $t = 8$ h for the calm synoptic wind case.

The adjusted surface pressure is defined as the deviation pressure π', minus π' at the far end of the water surface. Horizontal pressure gradients, the driving force for the sea breeze, are made more visible by this adjustment. The surface pressure is nearly uniformly low over the land before 4 h. In the early afternoon, the upward motion and movement of the isentropes in the updraft region become large, thereby creating a surface low-pressure center. This surface pressure dip intensifies as it moves inland. The surface pressure dip reaches its minimum value between 7 and 8 h and then begins to weaken and fill. The weakening of the low-pressure system on the surface in the mid-afternoon results from the decrease in the upward transport of heat, which subsequently weakens the circulation, as pointed out by Neumann and Mahrer (1974).

4) CORIOLIS DEFLECTION OF THE WIND

The Coriolis acceleration causes a clockwise rotation of wind in the Northern Hemisphere. Hodographs of the surface wind for the coast and 20 and 27.5 km inland are given in Fig. 8. At the shore, neither the formation nor the passage of the sea-breeze front occurs, so the magnitude of u simply increases to a maximum near 8 h, and then decreases. Because the Coriolis force always accelerates the wind toward its right, v simply increases with time to give a clockwise rotation of the surface wind (Fig. 8a). Both the formation and the passage of the front can be seen at 20 km inland (Fig. 8b); consequently, a change of sign of u appears twice between 5 and 7 h. The right sense of rotation is barely detectable during this time, but it is very obvious between 2 and 5 h and between 7 and 10 h. At 27.5 km inland, the clockwise rotation of the wind with time is clear: when u becomes more negative, v becomes more positive in the first 3 h; when u becomes positive and increases due to the formation of the front, v is decelerated to become more and more negative. Later, when u becomes less positive due to the approach (but not passage) of the front, v becomes less negative.

In summary, the Coriolis effect is correctly represented in our sea-breeze simulation. In the vicinity of the shore, the low-level wind over land turns clockwise with time. In the late afternoon, the along-shore component may become more than 50% of the normal-to-shore component of the surface wind such that the afternoon low-level wind has a substantially different direction from that of the morning wind. At stations inland, depending on their distance from the shore, the clockwise turning of the low-level winds with time may be considerably distorted by the formation and (or) the passage of the sea-breeze front. For this reason, the clockwise turning of the low-level winds toward the along-shore direction is not as obvious at a location far inland as in the vicinity of the shore.

5) SEA-BREEZE FRONT

In a sea-breeze model, the sea-breeze front generally is envisioned as a narrow horizontal area, ex-

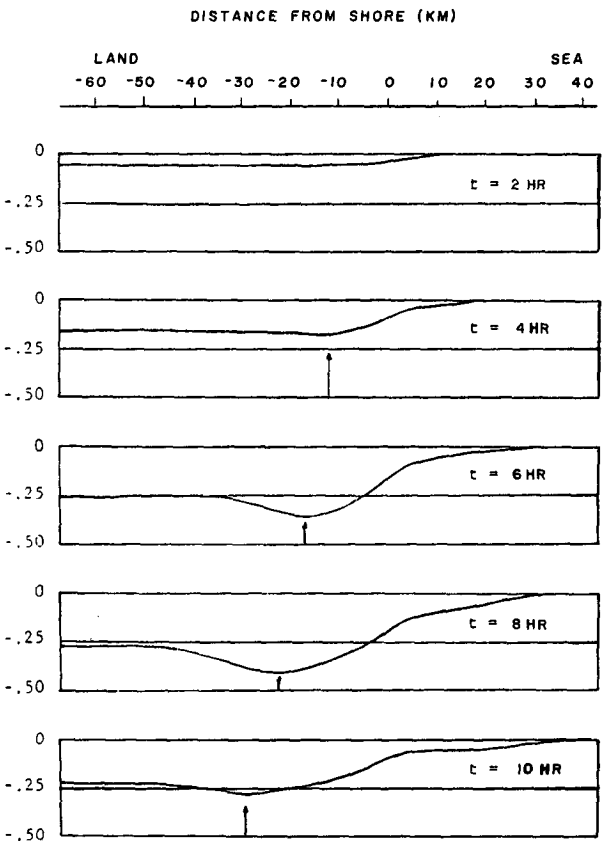

FIG. 7. The adjusted surface pressure $[m^2\ (K\ s)^{-1}]$ as a function of time and the distance from the coast. See text for the definition of the adjusted pressure. Arrows indicate the lowest surface pressure. Use the approximation 1 m^2 $(K\ s)^{-1}$ = 3.5 mb for unit conversion.

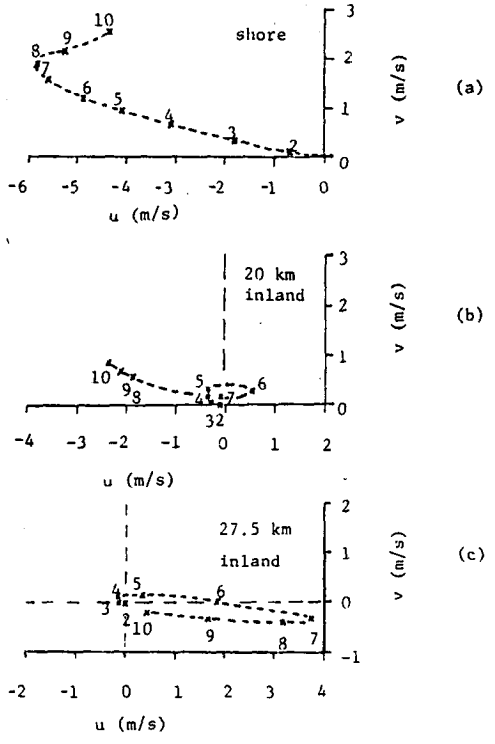

FIG. 8. Hodograph for three different horizontal sites for the calm synoptic wind case.

tending vertically from the surface, which separates the sea-breeze inflow from the land air. Therefore, the wind-shift line $u = 0$ can be used to represent the position of the front. Because of the rapid change of the u-velocity in the x-direction, a strong updraft is a characteristic of the sea-breeze front.

When the synoptic wind is calm, the low-level winds blow almost unidirectionally inland across the shore in the first few hours after the onset of the differential heating. During this period, the wind-shift line does not exist; the frontal position, therefore, is hard to define. For convenience, the location of the updraft center or the location of the surface low-pressure center can be used as an indicator of the surface frontal position.

The surface low-pressure center that is present by noon generates a region of offshore-blowing low-level winds some 20 km inland, thereby creating a well-defined sea-breeze front. Inasmuch as the inland offshore-blowing winds are obtained by a deceleration of the original onshore flow, it takes some time for the area of offshore flow to expand after the first appearance of such winds at low levels. For this reason, the front may temporarily appear to move backward toward the shore in its initiation stage.

To examine the inland movement of the sea-breeze front, hourly distances of the front from the shore are plotted in Fig. 9 for the three definitions of the front previously mentioned. Before 5 h, the front is not defined by either the wind-shift line or the surface low-pressure center. The dashed line gives the position of the updraft center for the first 5 h as an alternative frontal position. The entire w_{max} curve shows that, at 6 h, the inland velocity of the front decreases as the updraft strengthens. After the updraft has passed its peak value between 7 and 8 h and begins to diminish, the front regains an acceleration and moves inland faster. The other two curves also show that, near the mature stage of a sea breeze in the early afternoon, the frontal movement is relatively slow, but as the sea breeze begins to diminish, the movement of the front becomes faster.

This specific pattern of movement of the sea-breeze front (slow in the early afternoon to build up the strength of the circulation, and faster later in the afternoon as the circulation diminishes) also has been observed by Simpson *et al.* (1977) and modeled by Lambert (1974) and Stamm (1976). Other observational studies such as Lyons and Olsson (1973), and model results such as Pearson (1973), suggest either no significant change in frontal speed, or show a gradual slowing of the frontal movement in the late afternoon. Additional observational and theoretical studies are needed to clarify the details of the frontal movement in the late afternoon.

6) SEA BREEZE WITH A LIGHT OFFSHORE SYNOPTIC WIND

A 2.5 m s^{-1} offshore-blowing geostrophic wind was applied at the top of the model to study the synoptic-scale influence on the sea-breeze circulation. The most significant changes observed were in the intensity of the circulation and the characteristics of the front. From Fig. 10, it can be seen that, soon after the onset of the surface differential heating, the low-level offshore winds are weakened in the coastal area. The existence of an offshore synoptic wind evidently delays the formation of a layer of sea-breeze in-

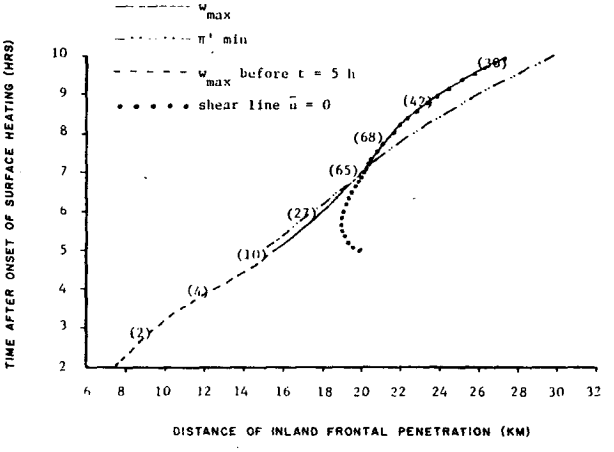

FIG. 9. Hourly inland-penetration distances of the sea-breeze front from the shore. Numbers in parentheses give the maximum vertical velocity in cm s^{-1} at each hour.

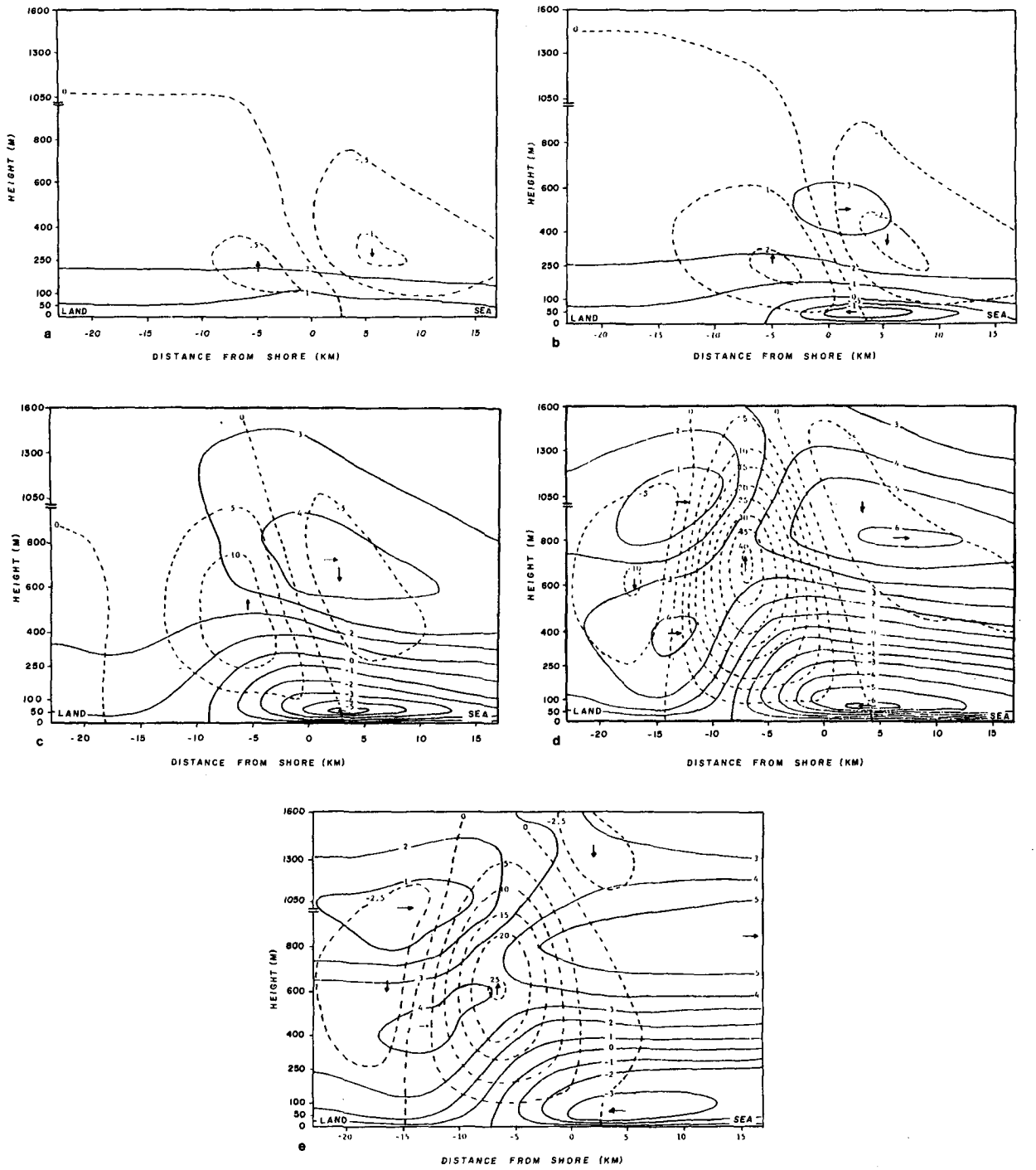

FIG. 10. Computed fields of u (solid line, m s^{-1}) and w (dashed line, cm s^{-1}) for the 2.5 m s^{-1} offshore synoptic wind case at (a) t = 2 h, (b) t = 3 h, (c) t = 5 h, (d) t = 7 h, (e) t = 9 h.

flow at low levels. The subsequent growth in size and strength of the inflow layer also is retarded by the offshore synoptic wind as compared with the calm case.

The onshore flow first appears slightly after t = 2 h, and moves inland until t = 5 h, but, in contrast to the calm case, the center of the maximum onshore flow never reaches the coast. The symmetry in strength and shape of the updraft and the downdraft that was evident in the first few hours for the calm case is not obvious in the presence of a synoptic wind. Also, the vertical extent of the inflow is less in the

current case. All these reveal the retardation effect of the offshore synoptic wind on the sea-breeze inflow.

A comparison of Fig. 10d with Figs. 4c, d, and e shows that the onshore wind speed and also the vertical gradient of wind speed near the surface over the water are greater when there is a weak, opposing synoptic-scale wind than when there is no large-scale flow. We are not aware of observations that might test this unexpected result. If this modeled result is physical and not an artifact of our turbulence parameterization, it could provide useful guidance to operators of pleasure and commercial boats in the coastal area. Results of simulations having larger opposing synoptic-scale flow show that the sea-breeze circulation with the resultant on-shore flow is not allowed to develop. Presumably, there is then a critical value for the opposing synoptic scale wind for which the onshore flow at the surface is maximum, all other conditions being equal (a stipulation that makes observational testing of this result difficult).

It also is clear from Fig. 10 that the sea breeze does not show an apparent correlation between the horizontal position of the maximum updraft and the wind-shift line near the surface in the first few hours of development. This indicates that the frontal zone is not well developed in the initial stage, which also was true for the calm case.

At $t = 5$ h in the calm case, a surface low-pressure center is induced by the updraft near the surface wind-shift line. The associated pressure gradient produces seaward-blowing winds at low levels. A similar mechanism causes the offshore winds at low levels ahead of the front to increase in the offshore synoptic wind case. Consequently, the inland movement of the shear line is significantly retarded, and the updraft dramatically increases to a maximum of $\sim$40 cm s^{-1} sometime between 7 and 8 h. Beyond this time, the decrease in the surface temperature begins to dominate and causes the vertical velocity to diminish.

By comparing Figs. 4 and 10, we see that the horizontal extent of the inland penetration of the sea-breeze inflow is considerably less than that for the calm case at any corresponding time. This demonstrates the significance of the retardation of the offshore synoptic wind. The maximum onshore wind in the inflow region at the mature stage of the sea breeze is, however, only 1 m s^{-1} less than that for the calm case.

In the absence of a synoptic wind, the u-field shows a four-cell pattern in the mature stage: an inflow cell between the coast and the front at low levels, a cell of return flow aloft, and a low-level seaward-blowing region ahead of the front, above which lies a cell of landward-blowing wind. In the presence of an offshore synoptic wind, the u-field is masked by the synoptic wind so that the upper-level winds always blow offshore.

Fig. 10 reveals that, in the presence of an offshore synoptic wind, the sea-breeze inflow region becomes sharper and shows a very slight recession between $t = 7$ and 10 h. This is very different from the inland advancement of the inflow in the late afternoon for the calm case.

The horizontal advection term in Deardorff's formula for the growth of the PBL tends to push the peak of the PBL height seaward. This increase in PBL height increases the model value of K_z throughout the entire vertical column above the surface layer, because the upper point for matching the cubic dependence of K_z has moved up. Therefore, the model K_z in and above the surface onshore flow region is increased simply because an elevated PBL height is advected in and not because of local changes in the turbulence. The resulting increase in vertical diffusion eventually weakens the onshore flow to the point that it is overpowered by the large-scale offshore flow. A more versatile turbulence parameterization is necessary for resolving the fine structure of the sea-breeze frontal zone, especially during the late afternoon when the convective PBL height loses its role as an appropriate turbulence parameter.

c. *Comparison with observations*

Lyons (1972) presented general characteristics of lake breezes based on 111 observed events. He described a typical lake breeze as resembling that observed near Chicago on 26 June 1967, which had an inflow depth of $\sim$500 m, a peak inflow speed of 6 m s^{-1}, return flow depth of $\sim$1500 m and peak velocity 4 m s^{-1}. There was a light (2–4 m s^{-1}) offshore synoptic wind on this day. The sea-breeze front penetrated to about 35 km by sunset. He also presented a time history of the vertical profile of horizontal wind speed at the shore and 35 km inland.

Comparison of these observations with our model results in Figs. 4, 9 and 10 show good agreement, except for the inland penetration of the front, which, for an offshore synoptic wind, is calculated to stay within 10 km of the shore. Our use of quite idealized surface heating and roughness and a simple turbulence parameterization could be factors contributing to these differences.

5. Concluding remarks

A 2-D finite-element PBL model has been developed and tested for both neutral and diabatic cases. With the simple Deardorff-O'Brien turbulence scheme, the model was able to give reasonable results in the simulations of a neutral PBL wind profile. Except for the detailed movement of the sea-breeze front in the presence of an offshore synoptic wind, the model also offers reasonable simulations of the sea breeze.

We intend to continue to refine the model by implementing other features of the finite-element method, by incorporating a more versatile turbulence

parameterization, and by applying the model to more challenging flow fields such as those created over complex terrain. Subsequent tests will be performed to determine whether the finite-element method has a significant advantage for these challenging flows.

Acknowledgments. We are grateful to Dr. J. C. Wyngaard and Dr. Otto Zeman for several helpful discussions on the turbulence parameterization, and Drs. P. M. Gresho, S. Chan and R. L. Lee of Lawrence Livermore National Laboratory, whose hydrostatic model forms the foundation of the present model. Acknowledgment is made to the National Center for Atmospheric Research, which is sponsored by the National Science Foundation, for computer resources used for this research. One of us (EST) wishes to acknowledge the National Science Foundation Faculty Professional Development Program for salary support during the initial stage of this research, and LPC wishes to acknowledge the Cooperative Institute for Mesoscale Meteorological Studies for salary support and drafting services during preparation of this manuscript. This material is based upon work supported by the Division of Atmospheric Sciences, National Science Foundation under Grant ATM 7923354.

REFERENCES

Businger, J. A., 1973: Turbulent transfer in the atmospheric surface layer. *Workshop on Micrometeorology*, D. A. Haugen, Ed., Amer. Meteor. Soc., 382 pp.

Chan, S. T., P. M. Gresho and R. L. Lee, 1980: Simulation of LNG vapour spread and dispersion by finite element methods. *Appl. Math. Model.*, **4,** 335–344.

Cullen, M. J. P., 1973: A simple finite element method for meteorological problems. *J. Inst. Math. Appl.*, **11,** 15–31.

Deardorff, J. W., 1974: Three dimensional numerical study of the height and mean structure of the heated planetary boundary layer. *Bound. Layer Meteor.*, **7,** 81–106.

Gresho, P. M., R. L. Lee and R. L. Sani, 1976: Modeling the planetary boundary layer using the Galerkin finite-element method. *Proc. Third Symp. on Atmospheric Turbulence, Diffusion, and Air Pollution*, Raleigh, Amer. Meteor. Soc., 82–89.

Haltiner, G. J., and R. T. Williams, 1980: *Numerical Prediction and Dynamic Meteorology*, 2nd ed. Wiley, 477 pp.

Hood, P., and C. Taylor, 1974: Navier-Stokes equations using mixed interpolation. *Proc. Int. Conf. on Finite Element Methods in Flow Problems*. University of Alabama Press, Huntsville, 121–132.

Huyakorn, P. S., C. Taylor, R. L. Lee and P. M. Gresho, 1978: A comparison of various mixed-interpolation finite elements in the velocity-pressure formulation of the Navier-Stokes equations. *Comput. Fluids*, **6,** 25–35.

Lambert, S., 1974: A high resolution numerical study of the sea breeze front. *Atmosphere*, **12,** 97–105.

Lee, H. N., and S. K. Kao, 1979: Finite-element numerical modeling of atmospheric turbulence boundary layer. *J. Appl. Meteor.*, **18,** 1287–1295.

Lyons, W. A., 1972: The climatology and prediction of the Chicago lake breeze. *J. Appl. Meteor.*, **11,** 1259–1270.

——, and L. E. Olsson, 1973: Detailed mesometeorological studies of air pollution dispersion in the Chicago lake breeze. *Mon. Wea. Rev.*, **101,** 387–404.

Manton, M. J., 1978a: A finite-element model of a moist atmospheric boundary layer: Part I. Model equations. *Tellus*, **30,** 219–228.

——, 1978b: A finite-element model of a moist atmospheric boundary layer: Part II. Method of solution. *Tellus*, **30,** 229–239.

Neumann, J., and Y. Mahrer, 1974: A theoretical study of the sea and land breezes of circular islands. *J. Atmos. Sci.*, **31,** 2027–2039.

O'Brien, J. J., 1970: A note on the vertical structure of the eddy exchange coefficient in the planetary boundary layer. *J. Atmos. Sci.*, **27,** 1213–1215.

Pearson, R. A., 1973: Properties of the sea breeze front as shown by a numerical model. *J. Atmos. Sci.*, **30,** 1050–1060.

——, 1980: Local flows. *Atmospheric Planetary Boundary Layer Physics*, A. Longhetto, Ed., Elsevier, 95–157.

Pielke, R. A., 1974: A three-dimensional numerical model of the sea breezes over south Florida. *Mon. Wea. Rev.*, **102,** 115–139.

——, and Y. Mahrer, 1975: Representation of the heated planetary boundary layer in mesoscale models with coarse vertical resolution. *J. Atmos. Sci.*, **32,** 2288–2308.

Sani, R. L., P. M. Gresho, R. L. Lee and D. F. Griffiths, 1980: The cause and cure (?) of the spurious pressure generated by certain FEM solutions of the incompressible Navier-Stokes equations. Rep. UCRL–84867, Lawrence Livermore Lab., 99 pp.

Shir, C. C., 1973: A preliminary numerical study of atmospheric turbulence flows in the idealized planetary boundary layer. *J. Atmos. Sci.*, **30,** 1327–1339.

Simpson, J. E., D. A. Mansfield and J. R. Milford, 1977: Inland penetration of sea-breeze fronts. *Quart. J. Roy. Meteor. Soc.*, **103,** 47–76.

Stamm, A. J., 1976: Comparison of lake breeze data with the Neumann-Mahrer non-hydrostatic numerical model. Ph.D. dissertation, University of Wisconsin, Madison, 154 pp.

Staniforth, A. N., and R. W. Daley, 1979: A baroclinic finite-element model for regional forecasting with the primitive equations. *Mon. Wea. Rev.*, **107,** 107–121.

——, and H. L. Mitchell, 1977: A semi-implicit finite-element barotropic model. *Mon. Wea. Rev.*, **105,** 154–169.

Wang, H. H., P. Halpern, J. Douglas, Jr., and T. DuPont, 1972: Numerical solutions of the one-dimensional primitive equations using Galerkin approximations with localized basis functions. *Mon. Wea. Rev.*, **100,** 738–746.

Wyngaard, J. C., O. R. Coté and K. S. Rao, 1974: Modeling the atmospheric boundary layer. *Advances in Geophysics*, Vol. 18A, Academic Press, 193–212.

Zeman, O., and H. Tennekes, 1975: A self-contained model for the pressure terms in the turbulent stress equations of the neutral atmospheric boundary layer. *J. Atmos. Sci.*, **32,** 1808–1813.

Zienkiewicz, O. C., 1977: *The Finite Element Method*, 3rd ed. McGraw-Hill, 787 pp.